

Towards Automatic Manipulation of Intra-cardiac Echocardiography Catheter

Young-Ho Kim^{1*}, Jarrod Collins^{1*}, Zhongyu Li², Ponraj Chinnadurai³, Ankur Kapoor¹,
C. Huie Lin^{2,4}, and Tommaso Mansi¹

¹Siemens Healthineers, Digital Technology & Innovation, Princeton, NJ, USA

²Houston Methodist Research Institute, Houston, TX, USA

³Siemens Medical Solutions Inc., Advanced Therapies, Malvern, PA, USA

⁴Houston Methodist DeBakey Heart & Vascular Center, Houston, TX, USA

Intra-cardiac Echocardiography (ICE) has been evolving as a real-time imaging modality of choice for guiding electrophysiology and structural heart interventions. ICE provides real-time imaging of anatomy, catheters, and complications such as pericardial effusion or thrombus formation. However, there now exists a high cognitive demand on physicians with the increased reliance on intraprocedural imaging. In response, we present a robotic manipulator for 4DOF ICE catheters to alleviate the physician's burden and support applied methods for more automated. Herein, we introduce two methods towards these goals: (1) a data-driven method to compensate kinematic model errors due to non-linear elasticity in catheter bending, providing more precise robotic control and (2) an automated image recovery process that allows physicians to bookmark images during intervention and automatically return with the push of a button. To validate our error compensation method, we demonstrate a complex rotation of the ultrasound imaging plane evaluated on benchtop. Automated view recovery is validated by repeated imaging of landmarks on benchtop and *in vivo* experiments with position- and image-based analysis. Results support that a robotic-assist system for more autonomous ICE can provide a safe and efficient tool, potentially reducing the execution time and allowing more complex procedures to become common place.

Index Terms—Intra-cardiac echocardiography (ICE), Catheter, Continuum manipulator, Tendon-driven flexible robot, Path planning, Automated View Recovery, Non-linear elasticity compensation, Cardiac Imaging

I. INTRODUCTION

Interventional cardiology has expanded its role dramatically in recent years to now encompass treatment of many disease states which were once considered to only have surgical options. This growth has been significantly motivated by the introduction of new treatment devices and advances in intraoperative imaging modalities. Intra-cardiac echocardiography (ICE) has been evolving as a real-time imaging modality for guiding interventional procedures in electrophysiology [1, 2, 3, 4], congenital [5, 6], and structural heart interventions [4], among others. When compared to another more established real-time imaging modality, transesophageal echocardiography (TEE), ICE has improved patient tolerance by not requiring esophageal intubation, requires only local anesthesia with conscious sedation, does not require an additional sonographer operator for imaging, and does not interfere with fluoroscopic imaging [7]. Real-time ICE imaging has an expanding role in providing uninterrupted guidance for valve replacement interventions [8, 9, 10, 11, 12, 13, 14, 15], left atrial appendage closure [16, 17, 18, 19, 20, 21], septal defect closure [22, 23, 24], and catheter-based ablation for cardiac arrhythmia [25, 26, 27, 28]. However, with the increased reliance on imaging to perform these complex procedures, there is a high cognitive demand on physicians, who now must perform both the interventional task and simultaneously acquire the guiding images. Moreover, they are not experts in

reading ultrasound and navigating these images, which makes ICE handling even more difficult.

ICE imaging requires substantial training and experience to become comfortable with steering the catheter to desired cardiac anatomical views, which hinders its adoption as standard of care [29, 13, 6]. In practice, the interventionalist is needing to continuously manipulate several catheters throughout the procedure, each having different control mechanisms. For example, a typical ablation treatment for cardiac arrhythmia can require tens to hundreds of individual ablations at very specific locations. ICE imaging can be beneficial for monitoring for developing complications, targeting anatomy, facilitating adequate tissue contact, and monitoring lesion development during ablations [26]. However, this can become an iterative and time-consuming procedure when frequently needing to re-position the therapeutic and imaging catheters. In structural heart procedures, clinicians can manipulate the ICE catheter to localize and measure the area of treatment and then either *park* (e.g. to watch for complications) or *retract* the ICE imaging catheter while devices are deployed under fluoroscopic guidance. The ICE catheter is then relocated to visually confirm the placement of therapeutic devices. This manner of repeated manipulation throughout the course of treatment is common for interventions across disciplines but requires intensive coordination, spatial understanding, and manual dexterity that can lead to fatigue in longer or more difficult procedures, imposes a significant learning curve for new users, and does not apply ICE imaging to its potential.

When considering these limitations, it is clear that a robotic-assist system to hold and actively manipulate the ICE catheter,

*Young-Ho Kim and Jarrod Collins are co-first authors. Corresponding author: Young-Ho Kim (young-ho.kim@siemens-healthineers.com).

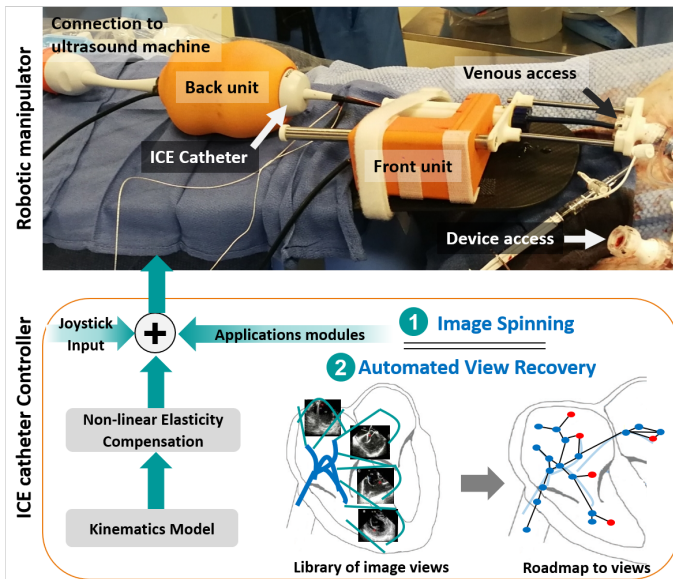


Fig. 1. An overview of the proposed ICE robotic manipulation.

either through an operator input or semi-autonomy, could ease the workload of the physician during treatment and potentially enable the use of ICE for novel and more complex procedures. Currently, there have been several commercial robotic systems to manipulate catheters on the market, including Amigo RCS (Catheter Precision, Inc., Mount Olive, NJ, USA), CorPath GRX (Corindus Inc., Waltham, MA), Magellan, and Sensei (Hansen Medical Inc., Mountain View, CA, USA). One commercially-available robotic system for ICE catheter manipulation is the Sterotaxis V-Sono system [30], which controls the ICE catheter robotically, but with limited degree-of-freedom. The main features are to provide robotic control of devices by human operators at the remote cockpit based on imaging (*e.g.* fluoroscopic) feedback. Loschak et al. [31] provide a method using electromagnetic (EM) tracking systems to accurately sweep the ultrasound imaging plane about a position, thus creating a way to actively maintain focus within the field of view. In further work [32] they apply a filtering method from EM sensors to compensate for respiratory motion. However, traditional sensors like EM cannot always be mounted at the tip of the catheter to provide required feedback due to practical limitations (*e.g.* cost, size, sterilization). While some ICE catheters are manufactured with an EM sensor in the tip for application in EP procedures, there is an accompanying increase in cost. In practice, many commercially available ICE catheters are single use with no sensors installed, therefore the controller for such a robotic-assist system requires an open-loop where spatial feedback are not continuously available. In this work, we apply a robotic catheter controller to enable control mechanisms which directly address the previously described challenges to standard use (*e.g.* repeated manipulation and cycling between views) in an open-loop control system (*i.e.* no additional sensors required).

In this paper, we introduce new methods to simplify ICE catheter manipulation for the interventionalist –both processes enabled by a robotic controller. Figure 1 shows an overview

of the proposed robotic-assisted system. More specifically, (1) We propose a data-driven method to compensate kinematic model errors due to non-linear elasticity fields in the bending planes that result from the catheter structure. With this, we demonstrate a method to spin the ultrasound imaging plane about the catheter axis while maintaining the catheter tip position, which also serves to evaluate the kinematics. (2) In response to limitations in current clinical ICE workflows, we propose an automated image recovery method which can reproduce important views that have been previously saved by the user during the procedure. We implement methods to incrementally generate a topological map, which facilitates to retrace a path to the specific view. We evaluated the proposed methods on benchtop and in a series of animal experiments.

The main contributions of this paper are:

- Data-driven models to compensate catheter kinematics for highly non-linear behaviors caused by the structural composition of the ICE catheter; these methods are evaluated with a practical learning method in the scenario of imaging while rotating about the catheter axis and maintaining a fixed catheter tip (*i.e.* image spinning) in benchtop studies.
- An automated view recovery method; we introduce a method to incrementally generate a topological map detailing the history of catheter motion during a procedure. When queried, the method provides a path to a specified view that can be reproduced at anytime by the robotic controller.
- The first known systematic evaluation of robotic ultrasound view recovery in *in-vivo* studies.

II. BACKGROUND AND RELATED WORKS

A. Kinematics and non-linear elasticity models of steerable catheters

An ICE catheter is a long, thin, and flexible structure, categorized as a continuum device. Two pairs of tendon mechanisms in the backbone control the ICE catheter tip which creates an underactuated system. Use of this flexible structure in practical applications requires models of robotic shape and motion, which is more complex than traditional rigid body robots. Several approaches exist to characterize positions, forces, and moments of the tip by actuators and external interactions with the environment. However, due to the complexities of modeling, most methods are solved numerically. As such, many publications have presented a simplified approach. The piecewise constant curvature approximation models the robot as a series of mutually tangent constant-curvature arcs [33], therefore providing closed-form kinematics and Jacobian formulation. There exist two mapping stages: one is from joint space to configuration parameters that describe constant-curvature arcs and the other mapping is from these configuration parameters to task space, consisting of a space curve which describes position and orientation along the backbone (detailed in Figure 2-3 in Robert J. Webster III [33]). Many continuum manipulators related to medical applications (*e.g.* endoscopes [34, 35, 36, 37], colonoscopes [38], catheters [31]) are composed of arcs. While imperfect, the constant curvature models are widely applied due to remarkable usefulness of the model approximation. In this work, we

apply the constant curvature model as a baseline. However, the existing ICE catheter is controlled by multiple tendons, which are coupled and have non-linear tensions due to polymer effects (detailed in Section III-A). As a result, the assumptions of the constant curvature model are invalidated; the effects of plastic torsion are neglected. Therefore, additional mapping functions are required to have concise control of the tip. There exist several works [34, 36, 37, 39] related to friction/hysteresis compensation in tendon-driven manipulators. Camarillo et al. [40] studied tendon configuration tracking methods to independently control the multiple sections of a catheter. Kato et al. [35] proposed the forward kinematic mapping method to compensate tension propagation due to hysteresis operation. Similarly, we construct an extended kinematic mapping function; however, focusing on compensation of non-linear elasticity in the bending plane.

B. Ultrasound Imaging and Automation

For some time, physicians have applied ultrasound imaging to observe, detect, and track target anatomies or surgical tools [41, 42] to great effect in a wide variety of procedures. Ultrasound image-based (semi-) autonomous robotic systems have been studied extensively for use in tracking the prostate for brachytherapy [43], to aid in target visualization and tool positioning for liver ablation [44, 45], to detect the tumour boundary in partial nephrectomy [46], and for catheter tracking in multimodal imaging [47].

Robotic catheter systems have been developed to improve maneuverability [31], compensate for the heart motion [32], and mapping for catheter navigation [48]. However, there are still many interventional processes that can benefit from the fast, repeatable, and precise controls that robotic manipulation can provide. Accordingly, we expect that the automated view recovery method presented in this work to be of high value to clinical ICE imaging.

III. MATERIALS AND METHODS

First, we present the ICE catheter mechanism, our robotic system, and we re-visit the existing kinematics models with our proposed compensation method. Then, we introduce our separate view recovery method.

A. ICE catheter mechanism

The ICE catheter structure has a highly nonlinear behavior due to various slack, elasticity, and hysteresis phenomena in multiple coupled components involved in tendon control. The mechanical composition of the ICE catheter (Figure 2 (a)) is based on two pairs of tendon-sheath pull mechanisms, which consist of a hollow polymer as a sheath and a thread sliding inside the sheath acting as a tendon. Each pair is bound to a common knob, which can pull an individual thread by rotating the knob, allowing one thread to be pulled while the other remains passive. This structure assumes ideally zero-slack transition between threads; however, this is not realistically achievable. Moreover, the ultrasound array is located in the center of the two pairs of tendon mechanisms which are

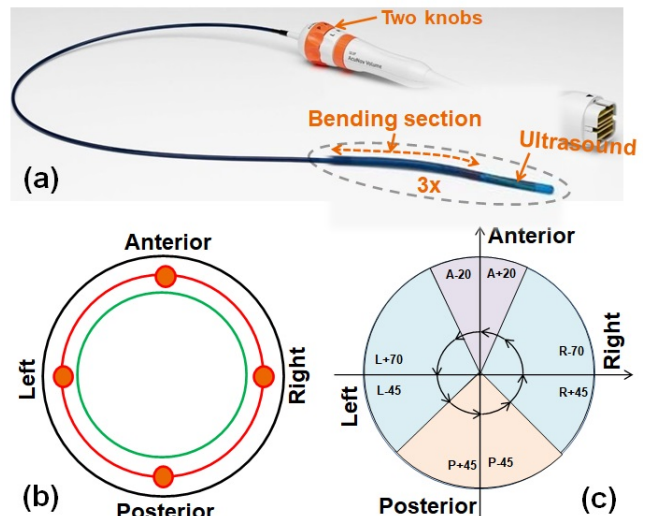


Fig. 2. (a) The ICE catheter is shown with two knobs, bending section, and ultrasound array labeled. (b) Catheter cross-section: four thread sections (orange) combining with polymer cover (black) and ultrasound array section (green), (c) Mechanical tolerance requirement

covered by the outer polymer shell for sterilization purposes (Figure 2 (b)). Highly nonlinear behaviors exist due to these structural considerations. Among others, we focus on plastic torsion due to complicated wires and tubes which we called non-linear elasticity that lead to the extreme mechanical tolerances presented in Figure 2 (c).

Precise prediction of the catheter tip pose for a specific knob configuration is therefore challenged by these non-linear properties. EM tracking systems have been used to co-localize the tip of the catheter in space. However, this increases the cost of the catheter and is currently only available, or clinically used, for EP procedures. In this paper, we investigate an open-loop control to address these challenges.

B. ICE catheter kinematics

We developed an ICE catheter robotic control system for this study. Our robot manipulator consists of two components as shown in Figure 1: 1) A “Front” component holds the catheter shaft, sits directly outside of the introducer sheath, and contributes linear and rotational motion of the catheter. 2) A “Back” component holds the catheter handle and controls the two knobs for the bending of the catheter tip, and bulk rotation of the catheter. Moreover, this bulk rotation is synchronized with the Front.

The robot has 4 degrees of freedom. Without loss of generality, we follow the same nomenclature from [31]: two DOFs for steering the catheter tip in two planes (anterior-posterior knob angle ϕ_1 and right-left knob angle ϕ_2) using two knobs on the catheter handle, bulk rotation ϕ_3 , and translation d_4 along the major axis of the catheter. We define the robot’s configuration, $\mathbf{q} = (\phi_1, \phi_2, \phi_3, d_4)$ in \mathbb{R}^4 . The robot can be controlled by manually using an external joystick, which provides a digital input that is directly mapped to the standard knob controls of the catheter or a more intuitive control scheme where the

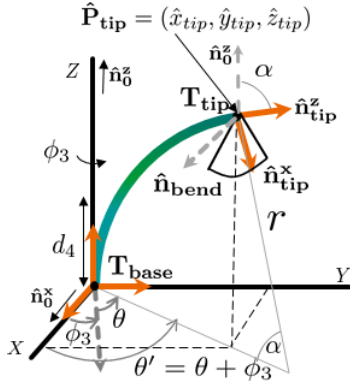


Fig. 3. Catheter bending geometry and kinematics nomenclature

users inputs are directly applied at the catheter tip coordinate frame.

For completeness, we summarize the explicit closed-form kinematics model based on [31]. The overall catheter bending geometry is described in Figure 3. To use constant curvature models, we setup the base coordinate frame T_{base} for the bottom of the bending section, and T_{tip} is the catheter tip coordinate frame where the ultrasound array is installed and the center of the image facing direction is \hat{n}_{tip}^x . The bending section length is defined as L .

Forward Kinematics (FK) from \mathbf{q} to T_{tip} :

There exist two configuration parameters in the constant curvature model, θ and α ; θ is the right-handed rotation angle from \hat{n}_0^x (the x -axis of T_{base}) along \hat{n}_0^z (the z -axis of T_{base}); α is the angle of the curvature, which is computed from anterior-posterior thread deflection, L_{ap} , and right-left thread deflection, L_{rl} . These thread deflections are normally computed from ϕ_1 and ϕ_2 with a knob radius r_{knob} as $L_{ap} = \phi_1 \cdot r_{knob}$ and $L_{rl} = \phi_2 \cdot r_{knob}$. Then, α can be computed as $\sqrt{\left(\frac{L_{ap}}{r_{catheter}}\right)^2 + \left(\frac{L_{rl}}{r_{catheter}}\right)^2}$, where $r_{catheter}$ is a catheter radius.

The remainder parts of kinematics as follows:

$$\theta = \tan^{-1}\left(\frac{\phi_2}{\phi_1}\right), \quad r = \frac{L}{\alpha} \quad (1)$$

$$\begin{aligned} \hat{x}_{tip} &= r (1 - \cos \alpha) \cos \theta, \\ \hat{y}_{tip} &= r (1 - \cos \alpha) \sin \theta, \\ \hat{z}_{tip} &= r \sin \alpha, \end{aligned} \quad (2)$$

More specifically, θ is the angle between the bending plane (due to ϕ_1 and ϕ_2) and the X-Z plane when $\phi_3 = 0$ (Figure 3). ϕ_3 will be added later. r is the radius of curvature in Equation (1). Then, the catheter tip position $\hat{\mathbf{P}}_{tip}$ is calculated from Equation (2).

The orientation of the tip can be calculated by the *Rodrigues' rotation formula*, which is a method for rotating a vector in space, given an axis and angle of rotation. Let $R(\mu, \beta)$ be the rotation matrix using *Rodrigues' rotation formula* from the given axis μ and rotating it by an angle β according to the right hand rule. Then, the orientation of the tip is computed by $R(\hat{\mathbf{n}}_{bend}, \alpha)$, where $\hat{\mathbf{n}}_{bend}$ is the vector orthogonal to the bending plane.

Let T_{tilt} be the 4x4 transformation matrix from $\hat{\mathbf{P}}_{tip}$ and

$R(\hat{\mathbf{n}}_{bend}, \alpha)$ without the body rotation ϕ_3 and translation d_4 . The rotation of ϕ_3 is $T_{roll}(\phi_3)$. The translation of d_4 is $T_{trans}(d_4)$. Then, the overall transformation matrix T_{tip} is given as $T_{trans}(d_4) \cdot T_{roll}(\phi_3) \cdot T_{tilt} \cdot T_{US}$ where T_{US} is the constant transformation from the tip of the bending section to the center of the ultrasound images along the catheter axis.

Inverse Kinematics (IK) from T_{tip} to \mathbf{q} :

Similarly, a closed-form solution of the inverse kinematics is as follows based on [31]:

$$\alpha = \cos^{-1}(\hat{\mathbf{n}}_0^z \cdot \hat{\mathbf{n}}_{tip}^z), \quad (3)$$

$$\theta' = \text{atan2}(\hat{y}_{tip}, \hat{x}_{tip}), \quad (4)$$

$$\hat{\phi}_3 = \theta' - \text{atan2}(\hat{\mathbf{n}}_{tip}^x \times R(\hat{\mathbf{n}}_0^x, \alpha), \hat{\mathbf{n}}_{tip}^x \cdot R(\hat{\mathbf{n}}_0^x, \alpha)), \quad (5)$$

$$\hat{\phi}_1 = \frac{\alpha \cdot r_{catheter} \cdot \cos(\theta)}{r_{knob}}, \quad (6)$$

$$\hat{\phi}_2 = \frac{\alpha \cdot r_{catheter} \cdot \sin(\theta)}{r_{knob}}, \quad (7)$$

$$\hat{d}_4 = \hat{z}_{tip} - r \cdot \sin \alpha, \quad (8)$$

α is the dot product of $\hat{\mathbf{n}}_0^z$ (the z -axis of T_{base}) and $\hat{\mathbf{n}}_{tip}^z$ (the z -axis of catheter tip) in Equation (3). The θ' is computed from the catheter tip position $\hat{\mathbf{P}}_{tip}$ in Equation (4). $\hat{\phi}_3$ is computed from the angle between $R(\hat{\mathbf{n}}_0^x, \alpha)$ (x -axis of T_{base} rotated by α) and the dot product of $\hat{\mathbf{n}}_{tip}^x$ (x -axis of T_{tip}) and $R(\hat{\mathbf{n}}_0^x, \alpha)$. The computed $\hat{\phi}_1$ and $\hat{\phi}_2$ represent the estimated joint states. We will compensate these for updated real values ϕ'_1 and ϕ'_2 . $\hat{\phi}_3$ is equal to ϕ_3 since the computed angle is given from the input. We assume here that other estimated joint states (ϕ_3 and d_4) are not affected by the non-linearity as the realization of these DOFs are also detached from catheter bending.

C. Non-linear elasticity compensation

Let $\mathbf{P}_{tip} \in \mathbb{R}^3$ be the real position ($x_{tip}, y_{tip}, z_{tip}$) of the catheter tip. When ϕ_1 and ϕ_2 are input to the kinematics model, the model predicted position $\hat{\mathbf{P}}_{tip}$ can present large discrepancies with the actual position \mathbf{P}_{tip} due to the effects of non-linear elasticity of the bending space. We assume that the bending length of the catheter remains constant due to the arc constraints, and then the two control knobs (*i.e.* anterior-posterior and right-left) cover the full working space. Accordingly, only $\hat{\mathbf{P}}_{tip}$ and \mathbf{P}_{tip} are misaligned as shown in Figure 4 (a). This is an inevitable consequence based on the mechanical tolerance data shown in Figure 2 (c).

To increase the accuracy of the kinematics model, we propose to map the model input (ϕ_1 and ϕ_2 for $\hat{\mathbf{P}}_{tip}$) with the real joint states (ϕ'_1 and ϕ'_2 for \mathbf{P}_{tip}). This mapping function is applied to both forward/inverse kinematics. We define the mapping function F as follows:

$$\phi'_1, \phi'_2 = F(\phi_1, \phi_2) \quad (9)$$

The function $F : \phi_1, \phi_2 \rightarrow \phi'_1, \phi'_2$ is the mapping function based on correcting the estimated position, $\hat{\mathbf{P}}_{tip}$ to the real position values, \mathbf{P}_{tip} . Each catheter has an individual model of elasticity behaviors within the catheter tolerance map as shown in Figure 2 (c).

The non-linear elasticity field learning method is addressed as follows:

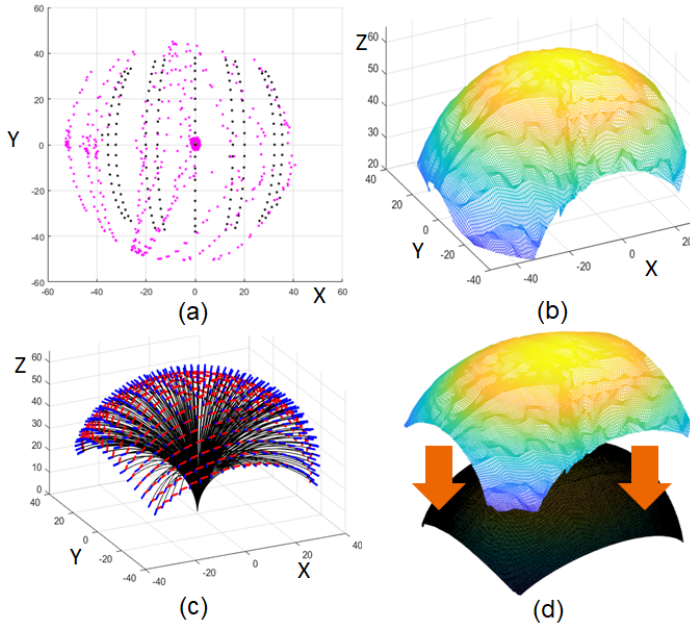


Fig. 4. This demonstrates one example of mapping procedures. The workspace is $\pm 90^\circ$. The bending length L is 60 mm . (a) This shows the bending plane X and Y corresponding to (ϕ_1, ϕ_2) ; the black dots indicate the model geometry $\hat{\mathbf{P}}_{tip}$ from forward kinematics model in 2D projection, the purple dots indicate the real geometry \mathbf{P}_{tip} in 2D projection, which are collected by EM sensors (10° intervals for $\pm 90^\circ$). The model geometry and the real geometry shows discrepancy due to non-linear torsion. (b) This shows interpolated \mathbf{P}^* corresponding to (ϕ_1, ϕ_2) on the T_{base} coordinate. \mathbf{P}^* is the unobserved values (i.e. the query points for interpolators). (c) This shows the estimated position $\hat{\mathbf{P}}_{tip}^k$ corresponding to (ϕ_1, ϕ_2) . This comes from the forward kinematics model. The red arrow indicates $\hat{\mathbf{n}}_{tip}^x$, while the blue arrow indicates $\hat{\mathbf{n}}_{tip}^z$. (d) We map the real geometry (b) into the model geometry (c) on T_{base} : both the black sphere ($\hat{\mathbf{P}}_{tip}$) and the colored mesh (\mathbf{P}_{tip}) are interpolated. Finally, the mapping function provides (ϕ'_1, ϕ'_2) corresponding to (ϕ_1, ϕ_2) .

First, we condition the model by collecting ground-truth data by manipulating the catheter by robot control and sampling the joint state (ϕ_1, ϕ_2) and the real position \mathbf{P}_{tip} . Then, we have S number of samples, which gives the real positions \mathbf{P}_{tip} related to (ϕ_1, ϕ_2) . Figure 4 (a) shows an example of the sampled ground-truth, \mathbf{P}_{tip} , as purple dots while $\hat{\mathbf{P}}_{tip}$ is shown as the black dots. There exist the model errors between the black dots and the purple dots due to plastic torsion.

Second, let $\mathbf{P}_j^* = (x_j^*, y_j^*, z_j^*)$ be the unobserved values based on the whole workspace ($[-d, d] \in \phi_1$ and ϕ_2), where d is the maximum degree of knobs, and $j \in U$, U is the number of unobserved values in the whole workspace. Then, we use a 2D interpolator with collected data to estimate \mathbf{P}_j^* . We have three interpolators: $(\phi_1^j, \phi_2^j) \rightarrow x_j^*$, $(\phi_1^j, \phi_2^j) \rightarrow y_j^*$, and $(\phi_1^j, \phi_2^j) \rightarrow z_j^*$. Figure 4 (b) shows an example of interpolated \mathbf{P}^* . We used the linear interpolator, which interpolated the value at a query point based on linear interpolation of the values at neighboring points in two-dimension. Several methods for interpolation exist (e.g. barycentric, polynomial, spline, etc).

Third, we applied the whole workspace inputs (ϕ_1^k, ϕ_2^k) , $k \in S + U$ into the forward kinematics model. Then, we get $\hat{\mathbf{P}}_{tip}^k$, which is shown in Figure 4 (c) as examples.

Lastly, we pick the query position $\hat{\mathbf{P}}_{tip}^k$, and find the nearest

position in $\mathbf{P}^* + \mathbf{P}_{tip}$. Then $(\phi_1^k, \phi_2^k) \rightarrow \hat{\mathbf{P}}_{tip}^k$ and $\hat{\mathbf{P}}_{tip}^k \rightarrow \mathbf{P}^* + \mathbf{P}_{tip}$, thus $\mathbf{P}^* + \mathbf{P}_{tip}$ give the corrected values (ϕ'_1, ϕ'_2) corresponding to (ϕ_1^k, ϕ_2^k) . As examples, we show the overall values in Figure 4 (d). Basically, we register the real geometry (\mathbf{P}_{tip}) to the model geometry ($\hat{\mathbf{P}}_{tip}$). The mapping function represents (ϕ'_1, ϕ'_2) corresponding to (ϕ_1, ϕ_2) .

We demonstrate non-linear elasticity compensation in the application of rotating the ultrasound image about the catheter axis, $\hat{\mathbf{n}}_{tip}^z$ (z-axis of the ICE catheter), while maintaining a constant tip position. This trajectory computation is possible using inverse kinematics. One example is that: (1) Initially, we start from $(\phi_1, \phi_2) = (60^\circ, 0^\circ)$, and rotate 360° along ϕ_3 . Then, the trajectory is one cosine function of ϕ_1 , one sine function of ϕ_2 , and one negative linear function of ϕ_3 . (ϕ_1, ϕ_2) example result is shown in Figure 5(a). These combined controls are challenging by hands, but robotic controls can provide easily.

D. Automated View Recovery: a topological map construction and path planning

During the procedure, we continuously construct a topological graph (“a roadmap”) and a library of views (i.e. important locations on the roadmap) based on the user’s trace and inputs when manipulating the catheter by joystick input to the robotic manipulator. Queries by the user to return to a specific view will be given to the controller to search a path. More specifically, let $\mathcal{G}(\mathbf{V}, \mathbf{E})$ represent a graph in which \mathbf{V} denotes the set of configurations \mathbf{q}_i and \mathbf{E} is the set of paths $(\mathbf{q}_i, \mathbf{q}_j)$. Our path planning is divided into two phases of computation:

Construction phase: The library of views and roadmap generation phase: as the robot moves, the current configuration \mathbf{q}_n is updated. If \mathbf{q}_n is not the same as the previous configuration \mathbf{q}_{before} , then the algorithm inserts \mathbf{q}_n as new vertex of \mathcal{G} , and connect pairs of \mathbf{q}_n and existing vertices if the distance is less than a density parameter ϵ (lines 10-12 of Algorithm 1). We apply ϵ based on Euclidean distance (assuming $1\text{ mm} \equiv 1^\circ$). If a larger ϵ (default = 1) were applied, then the search would be faster, however a safety of the path would not be guaranteed, as larger steps along the path could result in collision with anatomy. Concurrent with roadmap generation, the algorithm constructs a library of views \mathcal{V} when the user saves the view anytime, where $\mathcal{V} = (\mathbf{q}'_1, \dots, \mathbf{q}'_m)$, \mathbf{q}' is the user saved configuration. m is the number of the user saved views. This step is shown in line 16 of Algorithm 1.

Query phase: Given a start configuration \mathbf{q}_S (the current \mathbf{q}_n) and a goal configuration $\mathbf{q}_G \in \mathcal{V}$, is given during the procedures. Since each configuration is already in \mathcal{G} , we use a discrete A^* search algorithm to obtain a sequence of edges that forms a path from \mathbf{q}_S to \mathbf{q}_G . The more detailed roadmap construction and search algorithms in the graph are in [49].

The overall illustration of automated view recovery is shown in Figure 1: The roadmap to views and the library of image views are constructed in (construction phase; the blue dot shows the entire path of the user’s trace during joystick manipulation of the catheter; the red dot represents the bookmarked

Algorithm 1 BUILD_ROADMAP_VIEWS ($\mathbf{q}_n, \mathcal{G}, \mathcal{V}, \epsilon$)

```

1: INPUT: the current configuration  $\mathbf{q}_n$ , the current roadmap  $\mathcal{G}$ , the current library of views  $\mathcal{V}$ , the density parameter  $\epsilon$ 
2: OUTPUT:  $\mathcal{G}, \mathcal{V}$ 
3: Initialize:  $\mathbf{q}_{\text{before}} = []$ ,  $\mathcal{G} = []$ ,  $\mathcal{V} = []$ 
4: while ROBOT is OPERATIONAL do
5:    $\mathbf{q}_n$  is updated from the current configuration
6:   if  $\mathbf{q}_{\text{before}} \neq \mathbf{q}_n$  then
7:     for each  $q_i \in \text{NEIGHBORHOOD}(q_n, \mathcal{G})$  do
8:       if  $\text{dist}(q_i, q_n) \leq \epsilon$  then
9:         if  $q_n \notin \mathcal{G}$  then
10:           $\mathcal{G}.\text{add\_vertex}(q_n)$ 
11:        end if
12:         $\mathcal{G}.\text{add\_edge}(q_i, q_n)$ 
13:      end if
14:    end for
15:    if VIEW_SAVING_FLAG then
16:       $\mathcal{V}.\text{pushback}(q_n)$ 
17:    end if
18:     $\mathbf{q}_{\text{before}} = \mathbf{q}_n$ 
19:  end if
20: end while

```

or saved state of the robot when viewing a desired image (*i.e.* corresponding to the library of views). When applied during a procedure, the user can specify the desired view (red dot). The controller then identifies a path from the current configuration to the target configuration along the edges connecting the blue dots.

IV. EXPERIMENTS AND RESULTS

A. Experimental Design

1) Data-driven compensation model

Evaluation of the proposed compensation model was performed on benchtop. In this setup, we assume that the catheter is straight which allowed us to place the front component of the robotic manipulator near just below the bending section of the catheter to hold the catheter firmly (*i.e.* reducing the distance between catheter tip and the front component of the robotic manipulator to roughly 10 cm). We used three separate ICE catheters (ACUSON Acunav Volume, Siemens Healthineers) for all modeling and testing within this study.

Using an EM sensor attached to the tip of the ICE catheter, we collected the real position of the catheter in benchtop experiment while rastering the catheter along the full parameter space enclosed by $\pm 90^\circ$ in (ϕ_1, ϕ_2) (*i.e.* anterior-posterior and left-right control knobs). These data were then used to evaluate *baseline*, *brute-force*, and *practical* conditions of the compensation model. (1) The *baseline* condition uses the full discrete set of positional data collected during this exercise to produce trajectories based on \dot{P} . (2) The *brute-force* condition uses a dense set of ϕ_1 and ϕ_2 consisting of 360 samples collected at 10° intervals from the exercise to interpolate \mathbf{P}_{tip}^* and then generate trajectories based on \mathbf{P}_{tip}^* corresponding to (ϕ'_1, ϕ'_2) . (3) The *practical* condition similarly uses a sparse

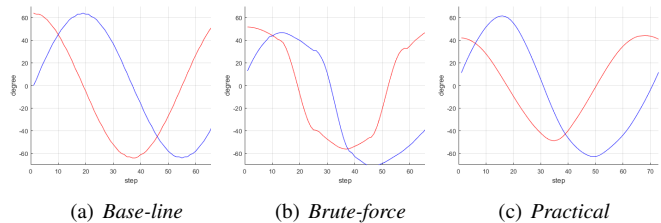


Fig. 5. This is the spinning simulation. The initial setup is $(\phi_1, \phi_2) = (60^\circ, 0)$. Y-axis is degrees. X-axis is time steps. (a) This shows the base model, so without any compensation. ϕ_1 and ϕ_2 are intercross each other. (b) The compensated ϕ'_1 and ϕ'_2 are demonstrated based on the densely collected data. (c) This shows the compensated ϕ'_1 and ϕ'_2 based on five points samples.

sampling of data from the workspace. To achieve the sparse sampling, we propose the simple training condition based on the tolerance map in Figure 2 (c). From our observation, the critical point is the boundary of the arc, which is the 90° from T_{base} for each bending side. Therefore, we pick five points experimentally that are easy to verify visually. Practically, we manipulate two knobs using the joystick to attempt the desired positions which are determined by (x_{tip}, y_{tip}) (*c.f.* z_{tip} is ignored due to arc constraints.). We propose five points: two 90° bending shape of the right-left planes when $x_{tip} = 0$, two 90° bending shape of the anterior-posterior planes when $y_{tip} = 0$, and finally the initial position by $(x_{tip}, y_{tip}) = (0, 0)$. After generating the motion trajectories, we applied the Savitzky-Golay filtering method to produce a smooth path. The chosen filter smooths according to a quadratic polynomial that is fit over each windowed trajectory. Three exemplary trajectories of the testing conditions are shown in Figure 5.

2) In vitro Study Design

Initial validation of robotic catheter control was performed on benchtop. An electromagnetic (EM) sensor (Model 800 sensor, 3D Guidance, Northern Digital Inc.) was attached to the catheter tip to provide real-time catheter tip tracking as the catheter was manipulated by robotic control for baseline evaluation of automated view recovery and image spinning methods.

3) In vivo Study Design

Three *in vivo* validation experiments were performed at the Houston Methodist Institute for Technology, Innovation & Education (MITIE, Houston Methodist Hospital) with the *in vivo* study protocol approved by the Institutional Animal Care and Use Committee (IACUC). All testing of the robotic catheter controller was performed under general anesthesia. Vascular access was achieved bilaterally to allow for manipulation of ICE and other device catheters. *In vivo* experimental setup is pictured in Figure 1. In each experiment, the ICE catheter, with robotic controller pre-attached, was introduced to the venous system through a 20F introducer sheath with balloon seal (DrySeal Flex Introducer Sheath, Gore) before being manually inserted to the junction of the inferior vena cava (IVC) and right atrium (RA) under fluoroscopic guidance. When viewing anatomy, ultrasound image data were recorded as DICOM format on an Acuson SC2000 (Siemens Healthineers). Dynamic computed tomography (DCT) images were acquired throughout experimentation on an Artis Zeego

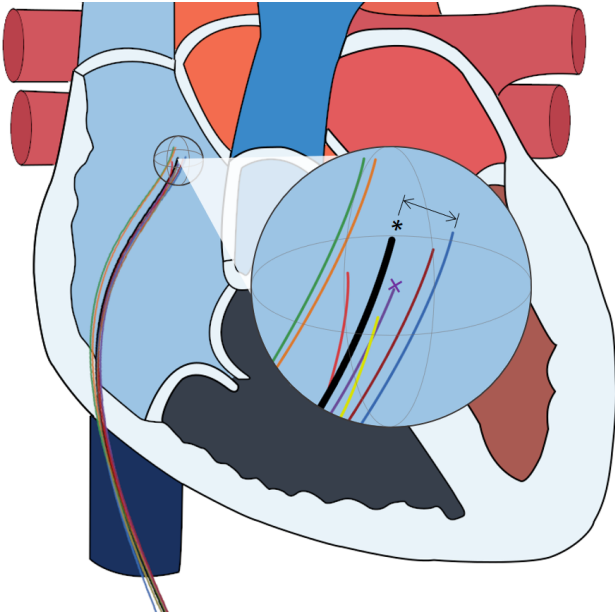


Fig. 6. Diagram of seven automated catheter returns to a single image-target. The black catheter, marked by *, represents the spatial average of the other seven. In this scenario, the purple catheter, marked by x, was designated as the reference catheter to which comparisons are made as it is the geometric median. The observed spread relative to the purple catheter represents the error associated with the automated view recovery as reported in this study.

(Siemens Healthineers) to provide volumetric ground-truth catheter localization relative to anatomy (200° total rotation, 5 second acquisition, 60 frames-per-second).

4) Validation metrics

For this study, we compare catheter tip location across multiple robotic positioning events to an image target as the primary spatial validation approach. For any catheter positioning to an image target, the robotic motors will theoretically return to an identical final state, assuming no slippage and consistent backlash. As we have created an open-loop system, when the robot executes movement along a path it is unaware of any external influences which may affect its final positioning. As such, any error in the positioning of the catheter tip are due to those external influences (*e.g.* catheter-robot mechanics, intravenous catheter interactions, cardiac motion, etc). These measurements, when taken relative to a reference catheter position, represent the distribution of uncertainty in robotic catheter positioning resulting from these external sources of error. Because of this, each experimental robotic positioning of the catheter to an image target can be considered a sampling of that uncertainty (Figure 6). Therefore, we have elected to use the geometric median catheter (*i.e.* the catheter which presented nearest the centroid of the sampled distribution) as the reference catheter for each imaging target when evaluating the automated view recovery method.

To measure *in vivo*, 3D models of the ground-truth observance of each ICE catheter were generated following an intensity-based threshold segmentation of intra-procedural DCT images (voxel spacing 0.498 mm) using ITK-SNAP [50]. Co-registration between DCT images were not necessary as no bulk patient motion was observed between scans. Next, the ICE catheter tip was manually labeled within each model

and the centroid taken to define the discrete tip location for a given robotic positioning event. A curve was then fit to each catheter, constrained to terminate at the predefined catheter tip, by automatically fitting a low-order polynomial. This process provided a discrete spatial representation of the catheter tip and body. Catheter tip localization error was calculated as the Euclidean distance between each resulting catheter tip location and the reference catheter tip location for a given imaging target.

Robotic catheter positioning was further validated by measuring the similarity of acquired ultrasound images between each experimental acquisition and the reference acquisition. Ultrasound image clips encompassing multiple heart cycles were acquired following each robotic positioning event. Image sequences were manually synchronized in time based on visible anatomy (*e.g.* valve leaflet position; from the first frame of the target valve being open to the last frame before reopening in the next cycle) and trimmed to encompass exactly one heartbeat. As before, image sequences from the geometric median catheter were selected as the reference images for comparison. Images for each series of target imaging events were then compared, in corresponding frames based on the heart cycle, to the reference images by computing the image cross-correlation. In-image regions of interest (ROI) were also manually labeled for each image series. ROI centroids from each image acquisition were measured to corresponding ROI centroids in the reference images by Euclidean distance.

B. Results

1) In vitro Evaluation of Image Spinning

The robotic controller was tasked with revolving the ultrasound imaging plane 360° about the catheter axis while maintaining a constant catheter tip position. This was performed from three initial conditions: a 20° anterior-posterior bend, a 40° anterior-posterior bend, and a 60° anterior-posterior bend (*i.e.* bending in ϕ_1). Under these conditions, the root-mean-square error (RMSE) catheter tip positional/rotational error from comparing the observed (EM tracking) and modelled (\hat{P}_{tip}) positions for the three model conditions and each model variance are addressed in Table I. Each cell of Table I is represented as (tip position RMSE, tip rotational RMSE), and the variance of model. These results represent that the *baseline* condition provides high bias and high variance. Conversely, the *brute-force* condition produces relatively low bias and low variance. Similarly, the *practical* condition also improves upon the *baseline* condition, providing lower bias and variance, but to a lesser extent than the *brute-force* condition.

2) In vitro Evaluation of Automated View Recovery

The robotic controller was tasked with cycling the ICE catheter tip through four target positions 18 times each to quantify the accuracy of robotic catheter control. Catheter tip positions requiring manipulation of all 4 DOF were established within the benchtop testing environment. These positions encompassed motion of up to 1.8 cm of translation, 51° whole body rotation, $\pm 51^\circ$ anterior-posterior bending, and $\pm 50^\circ$ left-right bending. Under these conditions, the RMSE catheter tip positional error was 0.5 mm and rotational error was 0.75° .

TABLE I
RMSE BETWEEN THE GROUND-TRUTH AND ESTIMATED POSITION/ROTATION DURING IMAGE SPINNING

Initial condition (ϕ_1)	20°	40°	60°
<i>Baseline</i>	(12.8 mm, 19.3°), 7.7 mm	(10.1 mm, 16.0°), 6.6 mm	(16.0 mm, 44.8°), 11.0 mm
<i>Brute-force</i>	(4.1mm, 19.4°), 4.2 mm	(5.6 mm, 20.8°), 4.8 mm	(6.5 mm, 24.8°), 5.2 mm
<i>Practical</i>	(6.5 mm, 20.3°), 4.3 mm	(7.99 mm, 24.44°), 5.2 mm	(10.0 mm, 27.0°), 7.2 mm

TABLE II
LOCALIZATION AND IMAGE-BASED VALIDATION DURING AUTOMATED VIEW RECOVERY

Image Target	Catheter Localization [mm]		Image Similarity [%]		ROI Localization [mm]	
	μ	σ	μ	σ	μ	σ
Aortic Valve	1.4	1.1	81.4	5.6	2.8	1.4
Mitral Valve	1.6	0.9	80.9	5.6	1.8	0.8
Tricuspid Valve	1.4	0.8	81.0	9.3	4.0	3.0

3) *In vivo* Evaluation of Automated View Recovery, Positional Analysis

Initial ultrasound views of the Aortic, Mitral, and Tricuspid valve imaging targets were manipulated by the physician using joystick input to the robotic controller (*i.e.* the joystick input maps to the standard catheter control knobs, these digital inputs are then translated to the robotic motors to result in catheter manipulation). For each target, the robotic control state was then added to the library of views for later automatic return via topological path planning. Views were then automatically returned to in series several times by automated robotic control (*e.g.* consecutively cycling through return to Aortic, return to Mitral, return to Tricuspid). The ultrasound image was recorded for several heart cycles and a DCT image was acquired for each viewing of an anatomical target. These data were then compared to measure the reproducibility of robotically controlled catheter motions. In total, three independent *in vivo* experiments evaluating automated view recovery were performed with four, six, and seven imaging events respectively per image target, resulting in 51 total view recoveries.

In animal catheter tip localization error from DCT is presented in Table II for each imaging target. Across all image-

targets, average catheter tip localization error was 1.5 ± 0.9 mm.

4) *In vivo* Evaluation of Automated View Recovery, Image Analysis

Example images from independent robotic re-acquisitions of the Tricuspid valve (*i.e.* unique imaging events) are presented in Figure 7 alongside the corresponding ground-truth catheter segmentations from DCT. Further examples of the Aortic and Mitral valves are presented in Figure 8. Image similarity as measured by image cross-correlation is presented in Table II for each image target. Average image similarity across all image-targets and experiments was 81.1 ± 6.9 %. For comparison and to establish an accuracy ceiling, average image similarity when comparing images from immediately consecutive heart cycles (*i.e.* without moving the catheter) was 89.8%.

Finally, in-image ROI were designated for each image target based on anatomy (Figure 7(A) and 8(A,C)). ROI centroids were then measured relative to corresponding reference ROI to quantify ROI localization error. Average in-image ROI localization error across all image-targets was 2.9 ± 2.2 . Again for comparison and to establish an accuracy floor, average ROI localization error when comparing ROI from immediately consecutive heart cycles (*i.e.* without moving the catheter) was 2.0 mm.

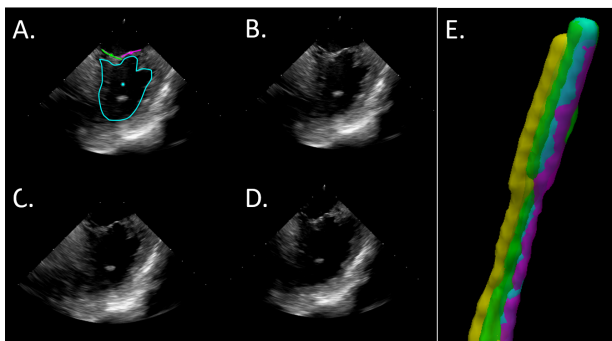


Fig. 7. Example results from *in vivo* validation experiments. (A) the initial view of the Tricuspid Valve from joystick control by the interventionalist. (B-D) reacquisitions by semi-autonomous robotic control of the ICE catheter. (E) presents the ground-truth catheter position of (A) in green and (B-D) in magenta, cyan, and yellow respectively. Manually labeled in-image ROI are also shown in (A).

V. DISCUSSION

The methods presented in this study represent the first work to demonstrate automated image recovery through robotic ICE catheter control. While there are several commercially available robotic catheter control systems on the market, there is only one commercial system, Vdrive (Stereotaxis Inc., St. Louis, MO, USA), which can provide limited manipulation of ICE catheters and one research prototype with a fully articulated 4 DOF [51]. In Brattain et al. [52], robotic methods were introduced for stitching together volumetric images of an ROI from 2D ICE images and tracking of a device catheter within images. Similarly, our work further advances ICE catheter robotics by augmenting the robotic control scheme with a spatially aware process to achieve more autonomous imaging; therefore, streamlining the user experience and allowing the

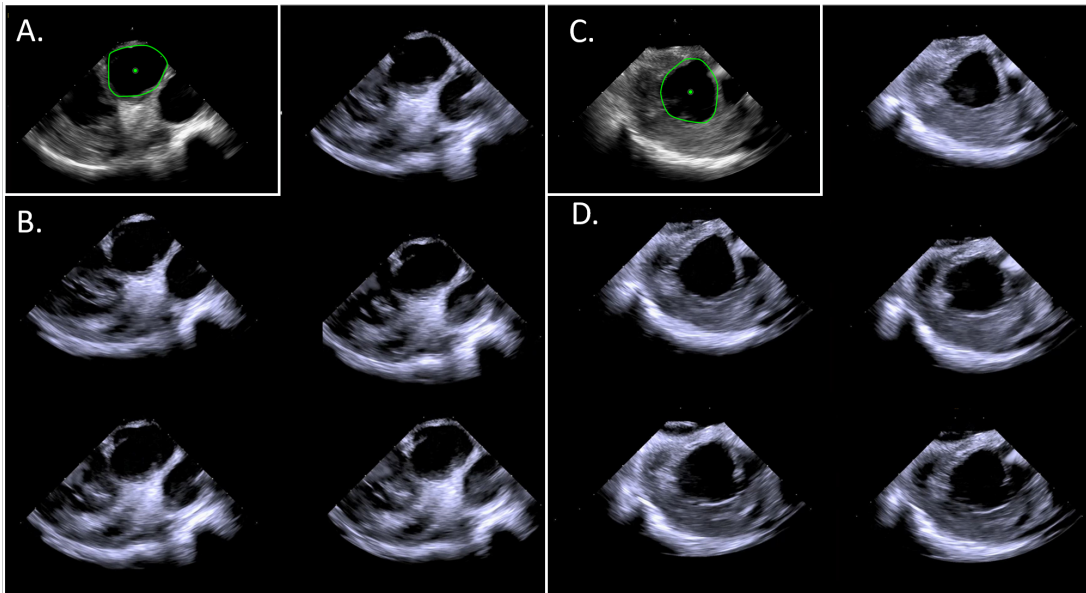


Fig. 8. (A,C) Reference and (B,D) automatically reacquired images of the Aortic and Mitral valves respectively. Manually labeled in-image ROI are shown in (A,C).

interventionalist to not divide focus throughout the procedure in order to image.

In this work, we apply a robotic ICE controller to implement a method for constructing a case-specific library of desired views and achieve automated recovery of those views during the procedure. In practice, standardized anatomical imaging views are emerging as indications for ICE continue to expand across disciplines. Enriquez et al. [53] detail standard imaging views for a variety of structural and electrophysiology procedures. Similarly, early identification and unobstructed monitoring of potentially life-threatening complications is one of the most valuable functions that ICE provides [22, 28, 54, 55] and is leading to its adoption as a primary imaging modality for certain procedures, especially those involving transseptal puncture for left heart catheterization [7, 56]. In response, we have developed the method presented in this paper to enable fast and precise cycling through selected views to both observe therapeutic delivery and monitor for procedural complications. If implemented in practice, these methods provide the interventionalist a means to initialize desired views covering the treatment area and then automatically return to those views at any point during a procedure. We have validated the accuracy of this approach in a series of animal experiments by a combination of spatial analysis (Figure 6) and image similarity measures (Figures 7 - 8).

Relative to typical right atrial measurements from echocardiography (3.6 ± 0.1 cm and 4.2 ± 0.1 cm for short- and long-axis respectively [57]), the level of catheter tip placement error observed in the automated view recovery *in vivo* experiments by DCT (*i.e.* 1.5 ± 0.9 mm) demonstrate high accuracy of by robotic catheter manipulations. These results are further corroborated by the *in vitro* catheter tip localization results acquired by EM sensing (*i.e.* 0.5 mm and 0.75°). However, we must note that the measurements taken *in vitro* are below the reported positional accuracy of the EM measurement sensor (*i.e.* 1.4 mm) but within the reported orientational

accuracy (*i.e.* 0.5°) and should be considered as such. In contrast, the *in vivo* validation measurements are well within the resolution of the DCT imaging. Comparing these *in vivo* and *in vitro* results demonstrates a compounding of error sources when moving between experimental settings which include: mechanical coupling of the catheter, robot, and sheath; interactions between the catheter and vascular anatomy; and physiological sources such as cardiac or respiratory motion. When considering the multiple sources of error and how they manifest in the catheter repositioning, it highlights a major limitation of our *in vivo* study design. Error accumulation affects not only the catheter tip position but also the orientation, or heading, of the ultrasound imaging plane. While we report high accuracy in tip positioning, we were unable to discretely measure misalignment of the imaging plane *in vivo*. As we see an increase in the positional error when moving from *in vitro* to *in vivo* settings (*i.e.* 0.5 mm to 1.5 mm), we would expect an increase in orientational error of similar magnitude. As a surrogate measurement, we present the image-based validation approaches. Figures 7 and 8 along with the similarity and ROI results in Table II represent a high degree of 2D spatial and content similarity in the produced images following robotic catheter manipulation. Altogether, we believe that these results support our conclusion that robotic controller and automated view recovery method introduced in this study are able to accurately position the ICE catheter within the RA and reproducibly image cardiac structures of clinical relevance. However, in future *in vivo* validation work, ground-truth validation of imager orientation should be collected by some means (*e.g.* EM sensing, measuring to anatomical targets in volumetric ICE image-data, or high resolution cardiac-gated cross-sectional imaging such as CT).

Safety is a major concern when considering any degree of robotic autonomy in human interfacing applications. As described, our automated view recovery method is not autonomously seeing views in an active manner, but rather rely-

ing on the user's initialization of each view and their tracing of possible paths (*i.e.* roadmap \mathcal{G}). As the user controls the ICE catheter during the procedure, they may cause the catheter to contact critical anatomies (*e.g.* septal wall, valves). However, the ICE catheter's end portion and tip are designed to be yielding so that the catheter will not puncture or damage tissue. With our presented semi-autonomous functionality, we rely on the user's previous navigation which we assume to conform with standard clinical practices. Furthermore, our spatial- and image-based results support that the robotic controller can maintain accurate and safe accordance with the expert user's trace.

As we mentioned in section III-A, there exist slack, elasticity, and hysteresis in the two pairs of tendons which mechanically drive the catheter. However, our methods are limited in that we are unable to separate and independently compensate these components. For example, as we collect benchtop data, hysteresis may occur when one tendon control knob is rotated, but slack may be present when the knob is near its zero or neutral position. Errors exist in the system because these phenomena are difficult to model and highly variable between different catheters. We can observe an interesting compensation in Figure 5(b). This represents an example of a trajectory from the *brute-force* condition. Here a relatively rough trajectory was observed even after filtering is applied. Specifically, rather steep slopes exist near the zero position, which may be able to compensate for slack. As expected, this is not visible in the *practical* condition due to the sparse sampling of training data. For the hysteresis, in our work, we did not separately collect the direction of the movement for ϕ_1 and ϕ_2 . In other words, if we make more interpolators considering directionality of data, it might be able to compensate hysteresis. However, this may require more densely sampled data, which means the *practical* condition might not be applicable due to real-world constraints.

It is also important that we discuss the magnitude of observed errors in Table I and Table II and to clarify the underlying studies. Table I presents results from image spinning in the benchtop setting with applied nonlinear elasticity compensation using the *baseline*, *brute-force*, and *practical* conditions. From the results in Table I, both the *brute-force* and *practical* compensation methods reduce model error and variance. However, there still exist errors even in the densely sampled, *brute-force* method. We hypothesize that these errors are due to slack and hysteresis which are not fully accounted for by the compensation model. Therefore, in future works, it may be important to integrate hysteresis modeling (*e.g.*, [37, 39]) alongside the proposed compensation method. In contrast, Table II presents *in vivo* validation of the automated view recovery approach. As described in Section III-D, this method does not rely on or apply the compensation method detailed in this work. View recovery is achieved by topological mapping of each motor state during joystick-defined manipulation of the ICE catheter by the user and subsequent pathfinding within the topological map to a desired image. In their current state, each method is applied in an open-loop scenario and represent independent initial steps towards an eventual closed-loop or more autonomous

navigation approach for ICE imaging.

VI. CONCLUSION

While ICE has many benefits when compared to other imaging modalities, it has limitations for clinical use largely due to difficulties in learning to control, produce, and interpret the ultrasound image. It is clear from these limitations that a robotic-assist system to oversee significant portions of procedural ICE usage could ease the workload and burden of the interventionalist, enable complex procedures that are currently impractical for vascular intervention, and reduce the overall resource burden of procedures by easing the transition from TEE to ICE imaging. We suggest that the field can be further advanced, and the driving clinical need better addressed, by augmenting the robotic controller with spatial- and image-based applications that provide direct input to the motor control loop and achieve more autonomous ICE imaging. Moreover, in our review of clinical literature, we have identified several natural use cases in standard ICE imaging that are synergistic with the application of advanced robotic control.

We believe that this work represents a meaningful advancement in the application of robotics for the challenging environment of intracardiac imaging. Herein, we present and validate in animal the first semi-autonomous ultrasound image recovery method for automating clinical ICE imaging in a natural use case. This work demonstrates that robotic control can be applied to accurately and reproducibly image in a systematic fashion. While further investigation is required to fully characterize and compensate the effects of various sources of error on both catheter kinematics modeling and *in vivo* catheter control, the evaluated methods appear promising. Based on this work, we recommend that the field of intracardiac imaging continue developing towards procedural automation and standardization which can be enabled through robotic assistance. We believe these data are supportive that robotic control can be reliably applied to automate standard processes within the clinical workflow.

DISCLAIMER

The concepts and information presented in this paper are based on research results that are not commercially available. The proposed system is currently under development. Due to regulatory reasons there future availability cannot be guaranteed. The scientists giving this presentation have a contractual relationship with Siemens Healthineers and have received financial compensation.

REFERENCES

- [1] L. Epstein, T. Smith, and H. TenHoff, "Nonfluoroscopic transeptal catheterization: safety and efficacy of intracardiac echocardiographic guidance," *Journal of Cardiovascular Electrophysiology*, vol. 9, no. 6, pp. 625–630, 1998.
- [2] E. Daoud, S. Kalbfleisch, and J. Hummel, "Intracardiac echocardiography to guide transeptal left heart catheterization for radiofrequency catheter ablation," *Journal of Cardiovascular Electrophysiology*, vol. 10, no. 3, pp. 358–363, 1999.

- [3] L. Calo, F. Lamberti, M. Loricchio, M. D'Alto, A. Castro, A. Boggi, and et al., "Intracardiac echocardiography: from electroanatomic correlation to clinical application in interventional electrophysiology," *Italian Heart Journal*, vol. 3, no. 7, pp. 387–398, 2002.
- [4] C. Basman, Y. Parmar, and I. Kronzon, "Intracardiac echocardiography for structural heart and electrophysiological interventions," *Current Cardiology Reports*, vol. 19, no. 10, p. 102, 2017.
- [5] G. Rigatelli, "Expanding the use of intracardiac echocardiography in congenital heart disease catheter-based interventions," *Journal of the American Society of Echocardiography*, vol. 18, pp. 1230–1231, 2005.
- [6] W. Tan and J. Aboulhosn, "Echocardiographic guidance of interventions in adults with congenital heart defects," *Cardiovascular Diagnosis and Therapy*, vol. 9, no. 2, pp. S346–S359, 2019.
- [7] F. Silvestry, R. Kerber, M. Brook, J. Carroll, K. Eberman, S. Goldstein, and et al., "Echocardiography-guided interventions," *Journal of the American Society of Echocardiography*, vol. 22, no. 3, pp. 213–231, 2009.
- [8] N. Green, A. Hansgen, and J. Carroll, "Initial clinical experience with intracardiac echocardiography in guiding balloon mitral valvuloplasty: technique, safety, utility, and limitations," *Catheterization and Cardiovascular Interventions*, vol. 63, no. 3, pp. 385–394, 2004.
- [9] T. Bartel, N. Bonaros, L. Muller, G. Friedrich, M. Grimm, C. Velik-Salchner, and et al., "Intracardiac echocardiography: a new guiding tool for transcatheter aortic valve replacement," *Journal of the American Society of Echocardiography*, vol. 24, pp. 966–975, 2011.
- [10] S. Ahmari, A. Amro, M. Otabi, M. Abdullah, S. Kasab, and H. Amri, "Initial experience of using intracardiac echocardiography (ice) for guiding balloon mitral valvuloplasty (bmv)," *Journal of the Saudi Heart Association*, vol. 24, no. 1, pp. 23–27, 2012.
- [11] K. Marmagkiolis and M. Cilingiroglu, "Intracardiac echocardiography guided percutaneous mitral balloon valvuloplasty," *Revista Portuguesa de Cardiologia*, vol. 32, pp. 337–339, 2013.
- [12] A. Henning, I. Mueller, K. Mueller, C. Zuern, T. Walker, M. Gawaz, and et al., "Percutaneous edge-to-edge mitral valve repair escorted by left atrial intracardiac echocardiography (ice)," *Circulation*, vol. 130, no. 20, pp. e173–e174, 2014.
- [13] T. Bartel, A. Edris, C. Velik-Salchner, and S. Muller, "Intracardiac echocardiography for guidance of transcatheter aortic valve implantation under monitored sedation: a solution to a dilemma?" *European Heart Journal of Cardiovascular Imaging*, vol. 17, no. 1, pp. 1–8, 2016.
- [14] M. Saji, A. Rossi, G. Ailawadi, J. Dent, M. Ragosta, and D. Lim, "Adjunctive intracardiac echocardiography imaging from the left ventricle to guide percutaneous mitral valve repair with the mitralclip in patients with failed prior surgical rings," *Catheterization and Cardiovascular Interventions*, vol. 87, no. 2, pp. e75–e82, 2016.
- [15] J. Patzelt, J. Schreieck, E. Camus, and et al., "Percutaneous mitral valve edge-to-edge repair using volume intracardiac echocardiography—first in human experience," vol. 1, no. 1, pp. 41–43, 2017.
- [16] H. Rao, S. Saksena, and R. Mitruka, "Intra-cardiac echocardiography guided cardioversion to help interventional procedures (ice-chip) study: Study design and methods," *Journal of Interventional Cardiac Electrophysiology*, vol. 13, pp. 31–36, 2005.
- [17] S. Shah, D. Bardo, L. Sugeng, L. Weinert, J. Lodato, B. Knight, and et al., "Real-time three-dimensional transesophageal echocardiography of the left atrial appendage: initial experience in the clinical setting," *Journal of the American Society of Echocardiography*, vol. 21, no. 12, pp. 1362–1368, 2008.
- [18] J. Ren, F. Marchlinksy, G. Supple, M. Hutchinson, F. Garcia, M. Riley, and et al., "Intracardiac echocardiographic diagnosis of thrombus formation in the left atrial appendage: a complementary role to transesophageal echocardiography," *Echocardiography*, vol. 30, pp. 72–80, 2013.
- [19] E. Anter, J. Silverstein, C. Tschabrunn, A. Schvilkin, C. Hafjajee, P. Zimetbaum, and et al., "Comparison of intracardiac echocardiography and transesophageal echocardiography for imaging of the right and left atrial appendages," *Heart Rhythm*, vol. 11, no. 11, pp. 1890–1897, 2014.
- [20] S. Berti, U. Paradossi, F. Meucci, G. Trianni, A. Tzikas, M. Rezaghi, and et al., "Periprocedural intracardiac echocardiography for left atrial appendage closure: a dual-center experience," *JACC Cardiovascular Interventions*, vol. 7, pp. 1036–1044, 2014.
- [21] Y. Matsuo, P. Neuzil, J. Petru, M. Chovanec, M. Janotka, S. Choudry, and et al., "Left atrial appendage closure under intracardiac echocardiographic guidance: feasibility and comparison with transesophageal echocardiography," *Journal of the American Heart Association*, vol. 5, no. 10, p. 4, 2016.
- [22] Z. Hijazi, Z. Wang, Q. Cao, P. Koenig, D. Waight, and R. Lang, "Transcatheter closure of atrial septal defects and patent foramen ovale under intracardiac echocardiographic guidance: feasibility and comparison with transesophageal echocardiography," *Catheterization and Cardiovascular Interventions*, vol. 52, no. 2, pp. 194–199, 2001.
- [23] M. Mullen, B. Dias, F. Walker, S. Siu, L. Benson, and P. McLaughlin, "Intracardiac echocardiography guided device closure of atrial septal defects," *Journal of the American College of Cardiology*, vol. 41, pp. 285–292, 2003.
- [24] B. Medford, N. Taggart, A. Cabalka, F. Cetta, G. Reeder, D. Hagler, and et al., "Intracardiac echocardiography during atrial septal defect and patent foramen ovale device closure in pediatric and adolescent patients," *Journal of the American Society of Echocardiography*, vol. 27, no. 9, pp. 984–990, 2014.
- [25] J. Kalman, A. Fitzpatrick, J. Olgin, and et al., "Biophysical characteristics of radiofrequency lesion formation in vivo : dynamics of catheter tip–tissue contact evaluated by intracardiac echocardiography," *American Heart Journal*, vol. 133, pp. 8–18, 1997.
- [26] W. Saliba and J. Thomas, "Intracardiac echocardiography during catheter ablation of atrial fibrillation," *Europace*, vol. 10, no. 3, pp. 42–47, 2008.
- [27] N. Bhatia, J. Humphries, K. Chandrasekaran, and K. Srivathsan, "Atrial fibrillation ablation in cor triatriatum: value of intracardiac echocardiography," *Journal of Interventional Cardiac Electrophysiology*, vol. 28, no. 2, pp. 153–155, 2010.
- [28] D. Filgueiras-Rama, F. de Torres-Alba, S. Castrejon-Castrejon, A. Estrada, J. Figueroa, O. Salvador-Montanes, and et al., "Utility of intracardiac echocardiography for catheter ablation of complex cardiac arrhythmias in a medium-volume training center," *Echocardiography*, vol. 32, no. 4, pp. 660–670, 2015.
- [29] N. Vitulano, V. Pazzano, G. Pelargonio, and et al., "Technology update: intracardiac echocardiography - a review of the literature," *Medical Devices (Auckland, NZ)*, vol. 8, pp. 231–239, 2015.
- [30] Stereotaxis, "Stereotaxis v-drive robotic navigation system," 2020, <http://www.stereotaxis.com/products/vdrive>.
- [31] P. M. Loschak, L. J. Brattain, and R. D. Howe, "Algorithms for automatically pointing ultrasound imaging catheters," *IEEE Transactions on Robotics*, vol. 33, no. 1, pp. 81–91, Feb 2017.
- [32] P. M. Loschak, A. Degirmenci, and R. D. Howe, "Predictive Filtering in Motion Compensation with Steerable Cardiac Catheters," in *Proceedings of the International Conference on Robotics and Automation*, Singapore, Singapore, May 2017.
- [33] B. A. J. Robert J. Webster III, "Design and kinematic modeling of constant curvature continuum robots: A review," *International Journal of Robotics Research*, vol. 29, no. 13, pp. 1661–1683, 2000.
- [34] L. Ott, F. Nageotte, P. Zanne, and M. de Mathelin, "Robotic

- assistance to flexible endoscopy by physiological-motion tracking,” *IEEE Transactions on Robotics*, vol. 27, no. 2, pp. 346–359, 2011.
- [35] T. Kato, I. Okumura, H. Kose, K. Takagi, and N. Hata, “Extended Kinematic Mapping of Tendon-Driven Continuum Robot for Neuroendoscopy,” in *Proceedings of the International Conference on Intelligent Robots and Systems*, Chicago, USA, Sep. 2014.
- [36] T. Do, T. Tjahjowidodo, M. Lau, T. Yamamoto, and S. Phee, “Hysteresis modeling and position control of tendon-sheath mechanism in flexible endoscopic systems,” *Mechatronics*, vol. 24, no. 1, pp. 12 – 22, 2014.
- [37] W. Xu, C. C. Y. Poon, Y. Yam, and P. W. Y. Chiu, “Motion compensated controller for a tendon-sheath-driven flexible endoscopic robot,” *The International Journal of Medical Robotics and Computer Assisted Surgery*, vol. 13, no. 1, p. e1747, 2017.
- [38] G. Chen, M. T. Redarce, and T. Redarce, “Development and kinematic analysis of a silicone-rubber bending tip for colonoscopy,” in *Proceedings of the International Conference on Intelligent Robots and Systems*, Beijing, China, Oct. 2006.
- [39] X. Wang, D. Bie, J. Han, and Y. Fang, “Active modeling and compensation for the hysteresis of a robotic flexible ureteroscopy,” *IEEE Access*, vol. 8, pp. 100 620–100 630, 2020.
- [40] D. B. Camarillo, C. R. Carlson, and J. K. Salisbury, “Configuration tracking for continuum manipulators with coupled tendon drive,” *IEEE Transactions on Robotics*, vol. 25, no. 4, pp. 798–808, 2009.
- [41] A. M. Priester, S. Natarajan, and M. O. Culjat, “Robotic ultrasound systems in medicine,” *IEEE Transactions on Ultrasonics, Ferroelectrics, and Frequency Control*, vol. 60, no. 3, pp. 507–523, 2013.
- [42] M. Antico, F. Sasazawa, L. Wu, A. Jaiprakash, J. Roberts, R. Crawford, A. K. Pandey, and D. Fontanarosa, “Ultrasound guidance in minimally invasive robotic procedures,” *Medical Image Analysis*, vol. 54, pp. 149 – 167, 2019.
- [43] J.-A. Long, N. Hungr, M. Baumann, J.-L. Descotes, M. Bolla, J.-Y. Giraud, J.-J. Rambeaud, and J. Troccaz, “Development of a Novel Robot for Transperineal Needle Based Interventions: Focal Therapy, Brachytherapy and Prostate Biopsies.” *Journal of Urology*, vol. 188, pp. 1369–1374, Aug. 2012.
- [44] E. Boctor, M. Choti, E. Burdette, and R. Webster, “Three-dimensional ultrasound-guided robotic needle placement: An experimental evaluation,” *International Journal of Medical Robotics and Computer Assisted Surgery*, vol. 4, no. 2, pp. 180–191, Jun. 2008.
- [45] J. Xu, Z.-z. Jia, Z.-j. Song, X.-d. Yang, K. Chen, and P. Liang, “Three-dimensional ultrasound image-guided robotic system for accurate microwave coagulation of malignant liver tumours,” *The International Journal of Medical Robotics and Computer Assisted Surgery*, vol. 6, no. 3, pp. 256–268, 2010.
- [46] R. Papalia, G. Simone, M. Ferriero, M. Costantini, S. Guaglianone, E. Forastiere, and M. Gallucci, “Laparoscopic and robotic partial nephrectomy with controlled hypotensive anesthesia to avoid hilar clamping: Feasibility, safety and perioperative functional outcomes,” *Journal of Urology*, vol. 187, no. 4, pp. 1190–1194, 2012.
- [47] X. Wu, J. Housden, Y. Ma, B. Razavi, K. Rhode, and D. Rueckert, “Fast catheter segmentation from echocardiographic sequences based on segmentation from corresponding x-ray fluoroscopy for cardiac catheterization interventions,” *IEEE Transactions on Medical Imaging*, vol. 34, no. 4, pp. 861–876, 2015.
- [48] Z. F. Issa, J. M. Miller, and D. P. Zipes, “6 - advanced mapping and navigation modalities,” in *Clinical Arrhythmology and Electrophysiology (Third Edition)*, third edition ed., Z. F. Issa, J. M. Miller, and D. P. Zipes, Eds. Philadelphia: Content Repository Only!, 2019, pp. 155 – 205.
- [49] S. M. LaValle, *Planning Algorithms*. New York, NY, USA: Cambridge University Press, 2006.
- [50] P. A. Yushkevich, J. Piven, H. Cody Hazlett, R. Gimpel Smith, S. Ho, J. C. Gee, and G. Gerig, “User-guided 3D active contour segmentation of anatomical structures: Significantly improved efficiency and reliability,” *Neuroimage*, vol. 31, no. 3, pp. 1116–1128, 2006.
- [51] P. M. Loschak, A. Degirmenci, Y. Tenzer, C. M. Tschabrunn, E. Anter, and R. D. Howe, “A four degree of freedom robot for positioning ultrasound imaging catheters,” *Journal of mechatronics and robotics*, vol. 8, no. 5, 2016.
- [52] L. J. Brattain, P. M. Loschak, C. M. Tschabrunn, E. Anter, and R. D. Howe, “Instrument tracking and visualization for ultrasound catheter guided procedures,” in *Workshop on Augmented Environments for Computer-Assisted Interventions*. Springer, 2014, pp. 41–50.
- [53] A. Enriquez, L. C. Saenz, R. Rosso, F. E. Silvestry, D. Callans, F. E. Marchlinski, and F. Garcia, “Use of intracardiac echocardiography in interventional cardiology: working with the anatomy rather than fighting it,” *Circulation*, vol. 137, no. 21, pp. 2278–2294, 2018.
- [54] S. S. Kim, Z. M. Hijazi, R. M. Lang, and B. P. Knight, “The use of intracardiac echocardiography and other intracardiac imaging tools to guide noncoronary cardiac interventions,” *Journal of the American College of Cardiology*, vol. 53, no. 23, pp. 2117–2128, 2009.
- [55] J. E. Banchs, P. Patel, G. V. Naccarelli, and M. D. Gonzalez, “Intracardiac echocardiography in complex cardiac catheter ablation procedures,” *Journal of interventional cardiac electrophysiology*, vol. 28, no. 3, pp. 167–184, 2010.
- [56] R. Bazaz and D. Schwartzman, “Site-selective atrial septal puncture,” *Journal of cardiovascular electrophysiology*, vol. 14, no. 2, pp. 196–199, 2003.
- [57] W. Bommer, L. Weinert, A. Neumann, J. Neef, D. T. Mason, and A. DeMaria, “Determination of right atrial and right ventricular size by two-dimensional echocardiography,” *Circulation*, vol. 60, no. 1, pp. 91–100, 1979.